Journal of Magnetism and Magnetic Materials 587 (2023) 171331

Contents lists available at ScienceDirect

Journal of Magnetism and Magnetic Materials

journal homepage: www.elsevier.com/locate/jmmm

The phase transformation behavior of Mn-Al rare-earth-free permanent magnets

Thomas Keller [a,*], Dylan Barbagallo [a], Natalya Sheremetyeva [a], Tushar Kanti Ghosh [b], Katherine S. Shanks [c], Geoffroy Hautier [a], Ian Baker [a]

[a] Thayer School of Engineering, 15 Engineering Drive, Dartmouth College, Hanover, NH 03755-8000, USA
[b] Université catholique de Louvain, 1 Place de l'Université, B-1348 Louvain-la-Neuve, Belgium
[c] Cornell High Energy Synchrotron Source, 161 Synchrotron Drive, Ithaca, NY 14853, USA

ARTICLE INFO

Keywords:
Mn-Al
Phase Transformation
Density Functional Theory
Electron Backscatter Diffraction
Synchrotron Diffraction
Ordering

ABSTRACT

Rare-earth-free permanent magnet materials based on Mn show great promise for applications in electric motors and devices. The metastable ferromagnetic τ phase of the Mn-Al system has magnetic properties between those of the high-performance Nd-Fe-B magnets and the lower-performance ferrite magnets. However, the hybrid displacive-diffusional pathway of τ formation, from the parent ε phase through the intermediary ε' phase, is still not fully understood. This phase transformation progression was studied *in-situ* using diffractive, calorimetric, and magnetometric techniques to show that the progression from ε to τ in $Mn_{54}Al_{46}$ at <450 °C involves the ordering of ε into ε'. Density functional theory calculations were performed on each phase and confirmed the experimental observation that the ε to ε' to τ pathway is energetically favorable. Isothermal annealing of quenched-in ε at 350 °C demonstrated that ε' is ferromagnetic, also in agreement with theoretical results, with a moderate coercivity of at least 50 kA/m. The τ phase was observed to nucleate along the prior ε phase grain boundaries and grow into the ε' phase regions. A boundary front of ε' was observed between the τ and ε phases. Both Kissinger and Flynn-Wall-Ozawa methods were used to determine the activation energies for the ε' and τ phase transformations with values of ~140 kJ/mol obtained for both phases. Therefore, the ordering transformation to ε' and the hybrid displacive-diffusional transformation to τ were shown to overcome the same magnitude energy barrier. Both activation energies were less than previous τ phase activation energies measured on $Mn_{55}Al_{45}$ in the absence of a significant ε' ordering exotherm, providing a kinetic benefit to the ε to ε' to τ pathway at 350 °C. The results of this study give insight into the phase transformation of $L1_0$ binary materials as well as materials that undergo a disorder–order transformation followed by displacive shear.

1. Introduction

The metastable ferromagnetic τ phase of the Mn-Al system has magnetic properties between those of the high-performance rare-earth (RE) magnets and the lower performance ferrite magnets. The ferromagnetic (FM) τ phase of the Mn-Al system is therefore a promising alternative to high-performance RE permanent magnets, such as Sm-Co and Nd-Fe-B, for use in electric motors and devices, and benefits from far lower raw material costs. Mn-Al magnets trade performance for material cost, and therefore for a given cost a larger volume Mn-Al magnet can be made to have the same performance as a Nd-Fe-B magnet ($(BH)_{max}$ in dollars per kJ/m^3) [1]. The τ phase has a metastable FM $L1_0$ ordered structure (P4/mmm space group; $a = 0.277$ nm, $c = 0.358$ nm in BCT and $a = 0.391$ nm, $c = 0.358$ nm in FCT) and is claimed to form through a hybrid displacive-diffusional phase transformation from the high-temperature ε phase, which has an HCP structure ($P6_3/mmc$ space group; $a = 0.2697$ nm, "b" $= 0.4671$ nm, and $c = 0.4396$ nm), as shown in the Mn-Al binary phase diagram (Fig. 1) and crystal structures (Fig. 2) [23]. The ordered B19 ε' phase has an orthorhombic structure (Pmma space group; $a = 0.276$ nm, $b = 0.458$ nm, and $c = 0.439$ nm), involving an expansion along the ε' a-axis of 2.3 % and a contraction along the ε' b-axis of 2.0 % [4]. However, the ε to τ phase transformation behavior is still the subject of debate, with conflicting ideas of the role of the ordering of the disordered HCP ε phase into the ordered B19 ε'phase. For example, the ordering of ε phase into ε' has been stated as a requisite step for ε to shear into τ and causes a reduction from six-fold symmetry

---

* Corresponding author.
E-mail address: Thomas.r.keller.th@dartmouth.edu (T. Keller).

https://doi.org/10.1016/j.jmmm.2023.171331
Received 11 July 2023; Received in revised form 6 September 2023; Accepted 27 September 2023
Available online 29 September 2023

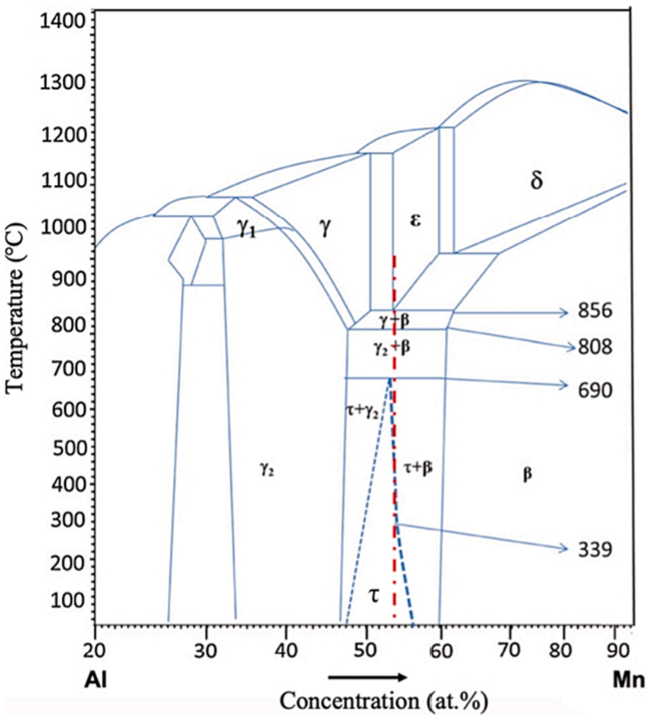

Fig. 1. Mn-Al binary phase diagram. From [23].

of the hexagonal ε phase to two-fold symmetry of the ε’ phase. This implies that there are three possible symmetry variants of ε’ that can nucleate relative to a parent ε phase orientation [5,6]. Three ε’ variants have been observed via TEM in the form of nanoinclusions (<10 nm) within a single ε matrix, confirming this relation [7,8]. The shear relation has also been confirmed by applying a uniaxial stress along the [1–11]$_{\varepsilon}$ direction of single-crystal ε to constrain the transformation to a single τ variant with the magnetically easy axis of [0 0 1]$_{\tau}$ parallel to the uniaxial stress [9].

The general consensus on the phase transformation, based on various *in-situ* and *ex-situ* TEM studies, is that both massive (diffusional) and shear (displacive) transformation modes are observed when quenched ε phase is heat treated in the temperature range of 450–750 °C [5,6,10–14]. The diffusional mode is claimed to dominate at temperatures above 600 °C whereas the displacive mode is claimed to dominate at temperatures below 600 °C, although evidence of both modes is generally observed concurrently at temperatures below 600 °C [15]. It has also been shown that cooling the ε phase at a controlled rate of 3.5–10 °C/s from >850 °C can transform it into the τ phase [16,17]. The ε’ to ε disorder temperature is in the range of 520–570 °C [18]. However, the phase transformation mechanisms at temperatures <350 °C are not well understood. Various *in-situ* characterization techniques have been used to investigate the phase transformation from ε to τ, starting with a quenched-in ε precursor and ramping at a constant heating rate to produce the τ phase while performing differential scanning calorimetry (DSC), thermal vibrating sample magnetometry (T-VSM), or high-energy X-ray diffraction (HE-XRD) [6,19–22]. The τ and ε phases are stable with ~3–6 at.% excess Mn above equiatomic composition, so $Mn_{54}Al_{46}$ is commonly used in experiments [1,23]. For example, Si *et al.* [6] used T-VSM to transform quenched-in Mn ε phase into τ and observed two distinct peaks of increased magnetic moment upon heating at 20 °C/min from room temperature to 600 °C [6]. This was suggested to be evidence of the two-modes of the ferromagnetic τ phase formation, with the displacive mode alone contributing the low-temperature peak and the massive mode alone contributing the high-temperature peak. Similarly, Genc *et al.* [22] performed DSC and HE-XRD on ε-phase $Mn_{53}Al_{47}$ and observed two exothermic peaks when heated at 10 °C/min from room temperature to 500 °C [20]. Their data suggested that the low-temperature peak was accounted for by the ordering into ε’ phase and the high-temperature peak was the formation of τ. They also observed a composition dependence for the ε’ phase ordering behavior, where for Mn-rich compositions greater than 55 at.% Mn ε’ phase did not form and ε phase decomposed into γ2 and β phases without forming τ. Therefore, the ε’ ordering behavior appears to be diminished in Mn-rich compositions. Activation energies for the τ phase transformation in previous studies have been measured for $Mn_{55}Al_{45}$ of 165 kJ/mol [2419] and 186 kJ/mol [21]. These studies did not report a significant ε’ ordering exotherm in their DSC data, likely due to the insignificant ordering observed at this composition. However, no study has combined the results from DSC, T-VSM, and HE-XRD to draw comprehensive conclusions about the thermodynamic, crystalline, and magnetic properties of the transformation and the intermediate ε’ phase.

This study clarifies the disagreements between the stated sources of two peaks in T-VSM and DSC data, i.e., whether they are evidence of the displacive τ phase formation or evidence of the ε’ ordering. Results from DSC, T-VSM, and HE-XRD were correlated and combined to understand the ε’ and τ phase formation behavior. Of key importance was the observation of two phase transformation events in the data using each *in-situ* technique, validating the growth of the ordered ε’ phase prior to τ. In addition, density functional theory (DFT) calculations were performed and compared to experiment to further justify the conclusions and the FM nature of the ε’ phase. A kinetic advantage due to lowered activation energies is shown for the ε to ε’ to τ phase transformation

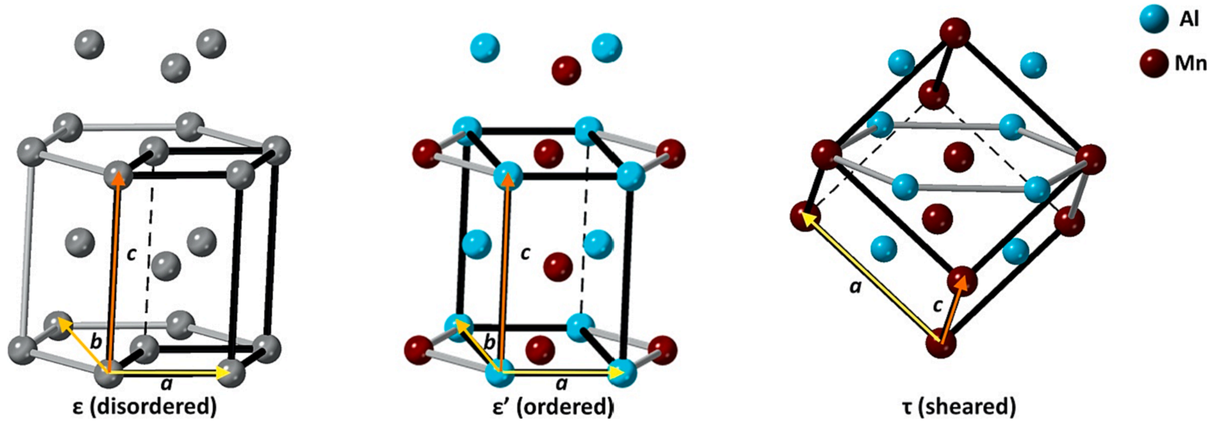

Fig. 2. The transformation from the parent A3 disordered ε phase to L1$_0$ τ phase (shown as FCT) through the intermediate B19 ε’ phase via the displacive shear transformation mode. Grey atoms in ε phase are of equal likelihood Mn and Al, black lines indicate the unit cell, and the hexagonal closed packed planes are shown in gray for reference. Redrawn from [14].

pathway at low temperatures.

2. Material and methods

A 5 kg ingot of composition $Mn_{54}Al_{46}$ was produced by Sophisticated Alloys, Inc. via induction melting. The sample composition was confirmed using scanning electron microscope (SEM) based energy dispersive spectroscopy (EDS) in a Tescan Vega3. Sections from this ingot (~0.5 g) were prepared by a 70 min homogenization anneal at 1100 °C in a sealed alumina tube to form the ε phase. The tube was evacuated to −85 kPa and backfilled with Ar gas to 15 kPa seven times prior to annealing in order to minimize oxidation. The annealed samples were immediately quenched in deionized water to preserve the ε phase at room temperature. Phase analysis was conducted using a Rigaku UltraX Cu-anode XRD (λ = 0.154 nm) to confirm the presence of the ε phase.

Annealed samples were prepared from the precursor ε phase by annealing at 350 °C for 1–20 h to observe the ε’ and τ phase evolution. Anneals were performed in a sealed alumina tube under Ar using the same method as above. XRD and VSM measurements were performed on these samples to observe the change in magnetic properties with associated changes in phase fractions. Rietveld refinement was performed using JADE software to determine the wt.% of each phase. Electron backscatter diffraction (EBSD) was performed using a Thermo Fisher Helios 5 SEM. EBSD samples were polished to a 0.05 μm finish using a Buehler Vibromet.

Samples of precursor ε were sectioned into ~0.05 g rectangular prisms, using a Buehler high-speed linear saw equipped with a diamond tip blade, for T-VSM and DSC analysis. Any oxide layer present on the samples was polished off using a sequence of 400–1200 grit Si-C paper on a rotary polishing wheel. T-VSM was performed in a Lakeshore 7300 VSM equipped with a heating oven under vacuum. A ramp rate of 5 °C/min under a 398 kA/m applied field was used to observe the transformation of ε to τ over a temperature range of 30–600 °C. DSC was performed in a TA instruments Q20 from 30 to 600 °C under flowing Ar. Ramp rates of 5–80 °C/min were used to perform the Kissinger and Flynn-Wall-Ozawa (FWO) methods of activation energy analysis [25].

For synchrotron XRD, samples of dimensions of 1 mm long, 2 mm wide, and 10 mm high were annealed and quenched to the ε phase in the same manner as the bulk samples. These samples were polished to a 1 μm finish using the aforementioned sequence of polishing paper as well as diamond polishing slurries. Synchrotron HE-XRD was performed at the Cornell High-Energy Synchrotron Source (CHESS) at Cornell University on the FAST beamline in the RAMS2 furnace. The sample was heated at a ramp rate of 10 °C/min from 30 to 650 °C with an incident beam energy of 41.991 keV (0.0295 nm). The sample temperature was measured at the sample surface using two attached thermocouples and averaged for each image. GSAS-II software was used to analyze the HE-XRD diffraction data and the diffraction conditions were calibrated with a CeO_2 reference sample. CrystalDiffract software was used to simulate the HE-XRD pattern.

3. Calculations

To model the relative energies and magnetic behavior of the ε, ε’, and τ phases, spin-polarized calculations were performed with density functional theory (DFT) as implemented in the Vienna Ab-initio Simulation Package (VASP) using the projector augmented wave (PAW) method and the generalized gradient approximation with the Perdew-Burke-Ernzerhof (GGA PBE) exchange–correlation functionals [26–29]. Unit cells of each phase were initialized with experimental lattice parameters [4,30] and fully relaxed with a cutoff energy of 520 eV for the plane-wave-basis set until the forces were less than 0.01 eV/Å. The convergence criteria of the electronic self-consistent field (SCF) loops were set to 10^{-6} eV. Monkhorst-Pack k-point grids were generated with a grid density of 2000 points per atom. To model the disordered ε phase, a 16-atom binary $Mn_{50}Al_{50}$ HCP special quasi-random structure (SQS) was generated using the Alloy Theoretic Automated Toolkit by considering pairs of atoms up to the tenth nearest neighbor and triplets up to the second nearest neighbor [31–35].

The Kissinger (Equation (1) [36] and FWO (Equation (2) [37,38] methods of activation energy are two methods based on an Arrhenius model of reaction rates and were applied using the procedures described in [39] and [25]:

$$\ln(\beta/T_{max}^2) = \{\ln(AR/E_a) + \ln[n(1-\alpha)^{n-1}]\} - E_a/RT_{max} \tag{1}$$

and

$$\log\beta = \{\log[AE_a/Rg(\alpha)] - 2.315\} - 0.457E_a/RT \tag{2}$$

where β is the DSC heating rate, T is the temperature, A is the Arrhenius factor, E_a is the activation energy, α is the degree of transformation, g(α) describes the transformation mechanism, n is the reaction order, and R is the molar gas constant. From DSC curves at various heating rates β, maximum exothermic peak temperatures were identified, and a plot constructed of $\ln(\beta/T^2)$ against −1/T. The slope of the ordinary least squares (OLS) regression line (E_a/R) was then calculated to solve for E_a via the Kissinger method. For the FWO method, each DSC exotherm was integrated at each β using a linear baseline and the transformed fraction, α, was correlated to the fractional area of the exotherm (see Fig. 3). The T at a given transformed fraction, α, was then used to plot log(β) against −1/T. The slope of the OLS regression line (0.457E_a/R) was then calculated to solve for E_a at each α via the FWO method. Thus, in both models only β, T, and α need to be measured experimentally and the calculation is independent of A, g(α), and n.

4. Results and discussion

4.1. DSC and T-VSM

DSC samples were ramped in temperature from 30 to 600 °C at a ramp rate of 10 °C/min. Two exotherms were observed, as shown in Fig. 3. The second (high-temperature) exotherm is confirmed in the overwhelming majority of experiments as arising from the formation of

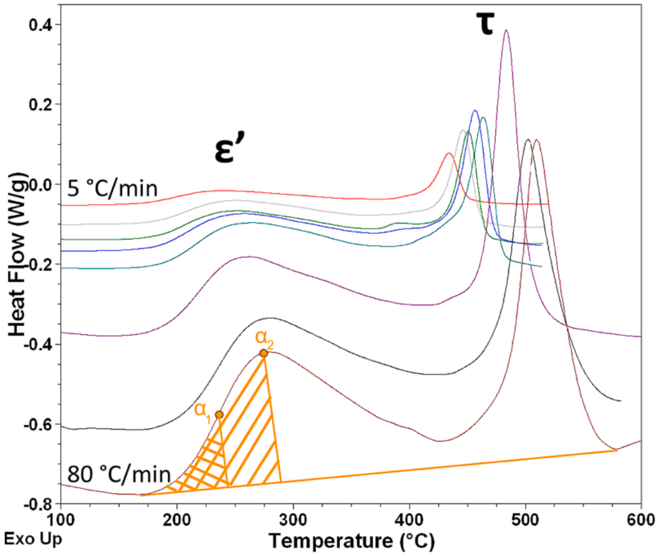

Fig. 3. DSC *in-situ* observation of the heat flow during heating from quenched-in ε to τ. From top to bottom the heating rates are 5, 10, 12, 15, 20, 40, 60, and 80 °C/min. Note the increase of the peak maxima temperatures with heating rate that were used in the Kissinger and FWO E_a calculations. The orange integrated areas show an example of two different transformed fractions, α, used in the FWO method.

the τ phase with a peak temperature around 450 °C [1]. However, the first (low-temperature) exotherm is largely omitted from studies of the τ phase formation, perhaps due to its unclear importance or the compositional dependence of ε' formation [13,19,21,22].

To compare the thermal behavior with magnetic behavior, T-VSM was performed under an applied field of 398 kA/m, ramping the sample from 30 to 600 °C at a ramp rate of 5 °C/min (the fastest ramp rate achievable on this T-VSM). The initial magnetism comes from the ε phase, which exhibits weak paramagnetism (PM) under the applied field (see Fig. 4). Two magnetic peaks were observed upon heating, implying the formation of two distinct phases arising out of the ε phase. The trend observed from 30 to 300 °C of decreasing magnetic moment, M, reflects the ε phase gradually losing magnetic alignment with the applied field due to increasing thermal perturbations of the magnetic dipoles. However, above 300 °C this trend reverses, and a peak develops, due to the formation of a new phase with a greater moment than ε at that temperature. This first peak is followed by a second peak, in good agreement with the DSC results. Therefore, the source of this low-temperature exotherm was studied to understand if its source was the beginning of the τ formation or the ordering of ε'. The T_C of the τ phase is ~375 °C but this is an extrapolation of the ideal behavior, and a fraction of PM moment is retained in real materials above T_C under an applied field. For example, roughly 3 % of the room temperature magnetization of the τ phase is retained at 450 °C under 398 kA/m. This explains the moment peaks in Fig. 4 even if the temperature exceeds T_C for the magnetic phase present. The phase transformation to a new phase with a higher FM or PM moment will create a peak followed by a loss of magnetization with increasing temperature. Therefore, the most likely explanation based on the data is that ε is transforming into two phases with greater FM or PM moments at the peak temperatures.

DFT modeling of the ε' phase unit cell was performed to determine if the lowest energy configuration of this phase was FM or antiferromagnetic (AF), as FM had been previously reported by Park *et al.*[40]. This demonstrated that FM is a lower energy configuration than AF by 36 meV/atom and that the first magnetic moment peak could be explained by either the FM ε' phase or the FM τ phase.

4.2. Synchrotron XRD

Therefore, HE-XRD was performed *in-situ* on $Mn_{54}Al_{46}$ during the ε to τ phase transformation. It is challenging to differentiate between the ε and ε' phases using conventional lab-scale Cu-anode XRD, because the similarity of their crystal structures results in significant overlap of the fundamental peaks. Yet, ε ordering into ε' results in a contraction along the [-1100] ε direction, thus some differentiation can be made by observing fundamental peak shift, as shown in the simulated pattern in Fig. 5 [4]. However, the clearest difference between the phases can be observed by the presence of the ε' [1 0 1] superlattice peak, which has no overlap with either ε or τ. Observing the phase transformation *in-situ,* the ε' phase indeed forms prior to τ upon ramping at 10 °C/min, and the ε' phase disappears concurrently with the formation of τ. A survey of the whole HE-XRD data is shown in Fig. 6 and in Fig. 7 the region of interest for the ε' and τ superlattice peaks is investigated in detail. At 125 °C and 200 °C, only single-phase ε is observed, as expected in the as-quenched material. At 315 °C, the initial evidence of the [1 0 1] and [0 1 0] superlattice ε' peaks begin to appear, coinciding with the DSC exotherm passing its maximum and the onset of the T-VSM peak. From 315 to 450 °C the ε' peaks grow in intensity without any evidence of the [0 0 1] τ superlattice peak. This therefore represents a period of nucleation and growth of the ε' phase prior to the formation of τ, and combined with the T-VSM data corroborates the FM behavior of ε' compared to ε. Above 450 °C the τ phase is shown to rapidly nucleate and grow in intensity, as evidenced by the [0 0 1] and [1 0 0] τ superlattice peaks, as well as the [1 1 0] and [0 0 2] fundamental τ peaks. This temperature agrees well with the second peak observed in both the DSC and the T-VSM data.

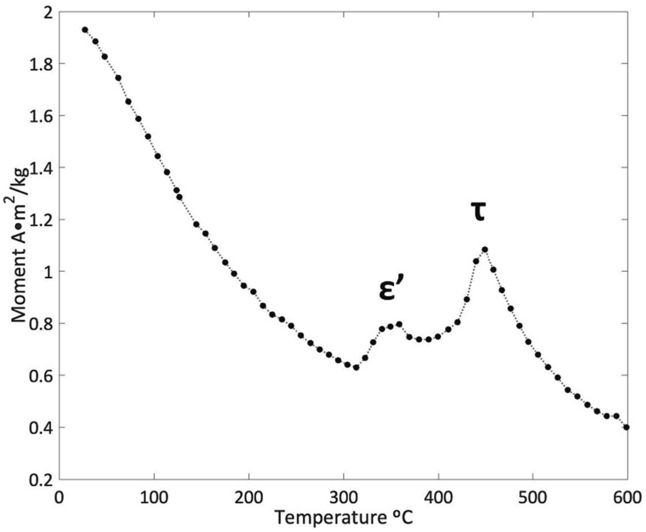

Fig. 4. T-VSM *in-situ* observation of the magnetic moment during heating from quenched-in ε to τ at 5 °C/min under a 398 kA/m applied field.

4.3. ε to ε' to τ phase progression at 350 °C

It is worth noting that although two peaks are observed in both DSC and T-VSM data, there is not a clear return to baseline between them. This implies that there is a region of overlap where the ε' formation is ending and the τ formation is beginning. This is confirmed in the HE-XRD data by the coexistence of ε' and τ phase superlattice peaks for a short time span, before all ε' is transformed to τ. This makes sense at these lower temperatures (~350 °C) considering the displacive mode of transformation, as τ can rapidly grow from existing ε' phase through shear while other regions are still undergoing ordering of ε into ε' through the slower diffusional process. To confirm this theory, samples of quenched ε phase were annealed at 350 °C to observe the phase evolution in this overlapping region. XRD analyzed via Rietveld refinement using JADE was performed on these samples to observe the phase evolution. The phase fractions are listed as a function of time in Table 1. Any phases, such as γ2 and β, determined to be present at less than 2 wt.% were considered within the margin of error and omitted from the analysis. The as-quenched sample is composed of 72 wt.% retained ε phase with 28 wt.% already transformed to ε'. This sample exhibits very low $M_{796kA/m}$ (using $M_{796kA/m}$ to mean the M observed at 796 kA/m as this material does not saturate fully at the maximum VSM field achievable) and H_{ci} (the coercivity measured on the M−H hysteresis curve). After a 1 h anneal the ordering transformation to ε' occurs, resulting in 79 wt.% of ε' at the expense of ε with no significant fraction of the τ phase observed. This 1 h anneal results in a small improvement to $M_{796kA/m}$ from 1.4 A•m^2/kg to 2.4 A•m^2/kg, but a substantial improvement in H_{ci} from 11.5 kA/m to 51.8 kA/m. Therefore, the ~1.8 times increase in wt.% ε' is accompanied by a ~4.5 times increase in H_{ci}. This is further evidence of the FM behavior of ε', demonstrating that significant magnetization is retained by this phase in the absence of an applied field. No significant fraction of τ greater than 1 wt.% was observed via XRD or EBSD that could increase H_{ci}. If a small τ phase fraction were affecting H_{ci}, previous studies of ~2 wt.% τ phase dispersed in a matrix of ε phase indicate that such a sample should have a coercivity greater than ~100 wt.% τ phase, due to the magnetic isolation of FM regions and the pinning of domain walls by the ε phase [41]. This is not the case for the 1 h sample, which has an H_{ci} of almost half the 6 h, 13 h, and 20 h majority-τ phase samples. Under an assumption that H_{ci} primarily arises from the magnetocrystalline anisotropy of the ε' phase in this case, and ignoring any effects from grain size changes, the ε phase, or crystalline defects, then this gives the first reported lower bound for H_{ci} due to the magnetocrystalline

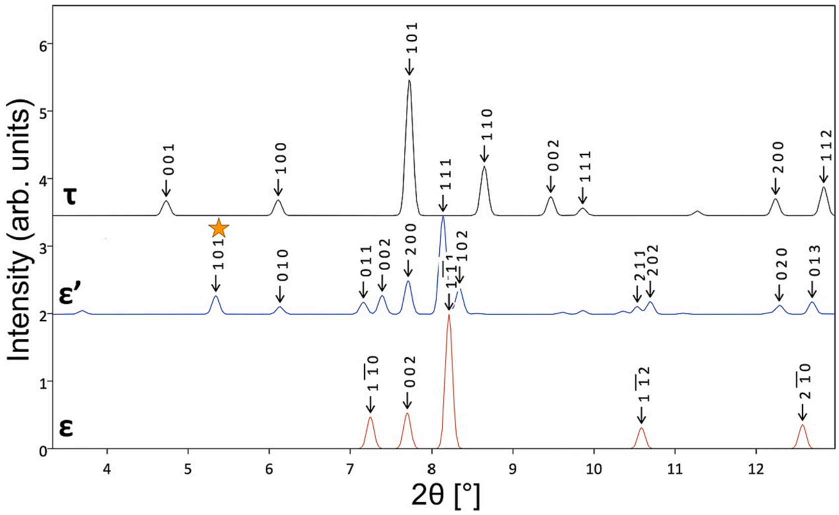

Fig. 5. Simulated HE-XRD pattern using lattice parameters from [4] at 0.02953 nm (41.991 keV). The [1 0 1] superlattice ε' peak is marked with an orange star.

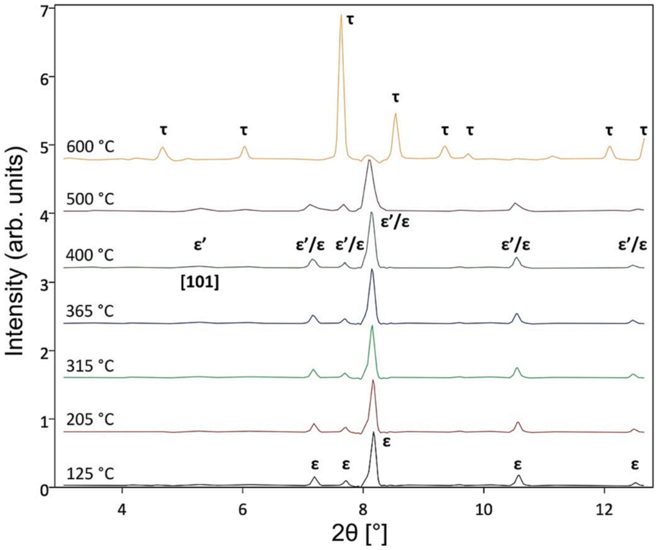

Fig. 6. HE-XRD *in-situ* observation of the $Mn_{54}Al_{46}$ phases present during heating from quenched-in ε to τ at 10 °C/min from 125 to 600 °C.

anisotropy of the ε' phase.

4.4. EBSD

EBSD was performed on the 1 h and 13 h samples annealed at 350 °C as shown in Figs. 8–12. Phase discrimination between the ε and ε' phases was possible due to the significant unit cell dimension change along the ordered ε' phase *a* and *b* axes compared to the ε phase. Fig. 8 confirms the transformation from majority ε phase to majority ε' phase, with the ε' dispersed throughout the existing ε grains. This agrees with TEM observations of ε' phase ordering as nanoinclusions within the matrix of an ε phase grain [7]. The orientations between ε and ε' phase variants agree with their symmetry relationship, e.g. $[0001]_{\varepsilon}$ parallel to $[0\,0\,1]_{\varepsilon'}$ [5,6]. A combination of strain from thermal stress during quenching and the lattice contraction associated with the ordering transformation accounts for the large voids that appear at the parent ε phase grain boundaries. Fig. 9 shows how the orientations of the ε phase regions are all the same within a particular grain. This is in contrast to Fig. 10, in which multiple ε' variants are present within the same parent ε phase grain. This is a strong indicator that the ε' variants are forming out of the parent ε phase. The selection of one out of the three possible ε' phase variants in a given ε phase grain is most likely due to stress retained from the thermal contraction of quenching as well as the stress between grains during the lattice contraction associated with ε' ordering. This is due to the anisotropic elastic properties of the ε' phase, making the ε' variant with a softer direction aligned to the stress more favorable than the others [7,10]. This explains why in some grain multiple variants are observed while in others one preferred variant has become dominant and is the only variant visible via EBSD. It is possible that all three variants are present in each grain at the nano-scale, in agreement with TEM studies, but only the preferred variant grows large enough to be visible. Nano-scale inclusions of ε' variants below the step size cannot be distinguished. The anisotropic elastic properties of the ε' phase may also explain why there is a grain of mostly retained ε phase present in Fig. 8. Unlike the surrounding grains, which are mostly transformed to ε' phase, this grain is disconnected from its neighbors via voids along its grain boundaries. Thus, it likely experiences less contraction stress from the surrounding grains and there is less strain energy to aid in the nucleation and growth of the ε' phase. Fig. 11a shows this grain in greater detail, demonstrating how the τ phase heterogeneously nucleates and grows out from the ε phase grain boundary, in agreement with previous TEM studies [5,8,10,12]. However, the benefit of EBSD in this case is that the ε and ε' regions (which are often referred to as a single ε/ε' region) can be differentiated down to the EBSD step size. Therefore, it is clearly shown that the τ phase grows into ordered ε' regions and not into disordered ε regions. For example, Fig. 11b shows several τ grains propagating behind ε' regions advancing into the parent ε grains. Nowhere in the samples was τ phase observed in direct boundary with the ε phase without a region of ε' phase separating them. This is additional strong evidence that the ordering process of ε into ε' facilitates the displacive transformation to τ at 350 °C, and agrees with the HE-XRD, DSC, and T-VSM results. Fig. 12 confirms that 13 h at 350 °C is sufficient to transform to τ and the grains show a high frequency of 76° "true" twins [7].

4.5. Comparing DSC with DFT

The ε to τ phase transformation was analyzed in terms of its activation energy, E_a, and exothermic change in enthalpy, ΔH, and the results compared to DFT calculations, as shown in Tables 2–4. As with any modeling, DFT cannot consider the full complexity of the phase transformation. A $Mn_{50}Al_{50}$ composition was used to avoid having to test the occupancy of the excess Mn antisite defects on Al sites to find the lowest enthalpy configuration for each phase as an SQS. However, since all

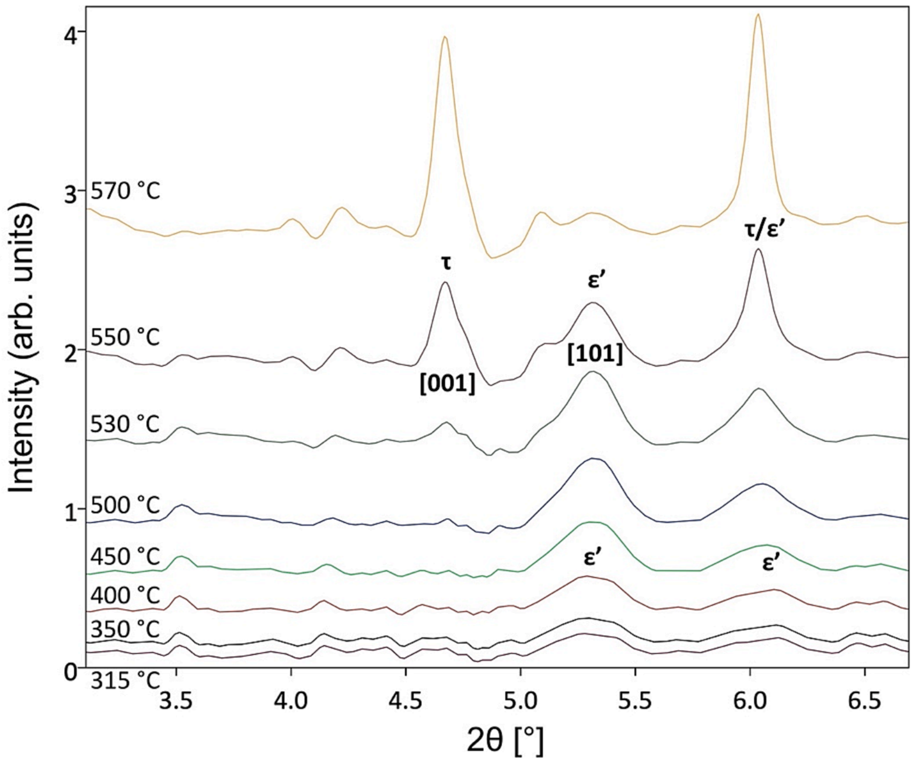

Fig. 7. HE-XRD *in-situ* observation of the $Mn_{54}Al_{46}$ superlattice peaks from 315 to 570 °C. This temperature range covers the onset of the ε' formation and the onset of the τ transformation.

Table 1
Effects of annealing at 350 °C for various times on the magnetic properties and phase fractions of quenched ε $Mn_{54}Al_{46}$.

Time (h)	$M_{796kA/m}$ ($A\bullet m^2/kg$)	H_{ci} (kA/m)	ε wt. %	ε' wt. %	τ wt. %
0	1.4	11.5	72 ± 3	28 ± 3	–
1	2.4	51.8	21 ± 2	79 ± 3	–
6	37	92.9	–	13 ± 1	87 ± 1
13	64	93.3	–	–	96 ± 2
20	65	92.9	–	–	96 ± 3

three phases were modeled at the same composition, the contribution from the lack of Mn antisite defects was mitigated. Furthermore, DFT cannot account for the influence of other defects, such as twins, APBs, stacking faults, and dislocations, that are known to play a role in the transformation from ε phase to τ phase and could change the enthalpy of the system. Last, all three phases were modeled as infinitely large single-crystals, whereas the experimental samples were all polycrystalline, therefore inter-granular effects observed in the ε' phase EBSD results, such as stress, coherence to the parent phase, and competition between variants, could not be considered.

Using the model of the phase transformation described in [42] the activation energy is treated as the energy barrier which must be overcome to proceed from the parent ε phase to ε' and thus from ε' to τ. DFT confirms that, energetically, the progression from ε to ε' to τ is favorable, with the energy per atom decreasing with each step of the phase transformation. This agrees with the negative ΔH observed experimentally. Thus, ε' is the most likely source of the low-temperature exotherm. The ΔH predicted by DFT calculation is ~2–5 times greater than the experimental ΔH measured by DSC and the ΔH calculated for ε' phase is ~3 times greater than for τ. However, there are some reasonable explanations for this difference. First, the DFT calculation assumes a transformation from disordered ε to fully ordered ε', but partial ordering would result in a smaller ΔH. The XRD results indicate that some ε' is present after quenching, which would diminish the ΔH measured experimentally since some partial ordering has already occurred. From the EBSD data, multiple competing ε' regions are shown to form within existing ε grains (Fig. 10). Regions consisting of many small neighboring ε and ε' phase regions (green and blue pixels) are demonstrating only partial long-range ε' ordering (LRO). A parallel argument can be made for the incomplete ordering of the τ phase during DSC measurements leading to an under-measurement of the ΔH compared to the DFT calculation. Second, ε grain boundaries are shown to have τ phase heterogeneously nucleate on them, followed by τ phase growth into the ε' variants, preventing large ε' phase volume fractions from fully ordering before transforming to τ. Therefore, the combination of existing ε' phase in the as-quenched material, ε' variant competition within ε phase grains (poor LRO), and the transformation to τ before complete ε' ordering can occur are all explanations for why the ΔH measured for ε' is less than the calculated energy for an ideal disorder–order transformation. Third, as is reflected in the EBSD, DSC, VSM, and HE-XRD data, there is not a distinct delineation between the ε to ε' and ε' to τ transformations. Rather, the two transformations are shown to overlap, with some fraction of ε' transforming to τ while ε to ε' ordering is still occurring. Therefore, it is difficult to precisely distinguish between the relative contributions to ΔH from each transformation. The measured ΔH sum of both transformations is ~7 kJ/mol, which is in reasonable agreement with the calculated ~6 kJ/mol contribution from τ and a fractional calculated contribution from ε' (~20 kJ/mol) if only partial ordering occurs. Lastly, given that these are all metastable phases at room temperature, there will always be some interference from decomposition to the equilibrium phases γ2 and β shown in Fig. 1, although the effects should be minimal below 600 °C.

DFT calculations also indicate that the magnetic moment of the ε phase is 93 % that of τ. However, in the 350 °C anneal progression the magnetization observed from the 1 h ε' phase-majority sample is roughly 4 % of the 20 h τ sample. Nevertheless, this calculation is performed at 0 K, and therefore the discrepancy could be explained by ε' having a significantly lower T_c than τ (T_c for τ = ~375 °C). Observation of T_c for this phase experimentally is difficult, due to the metastable

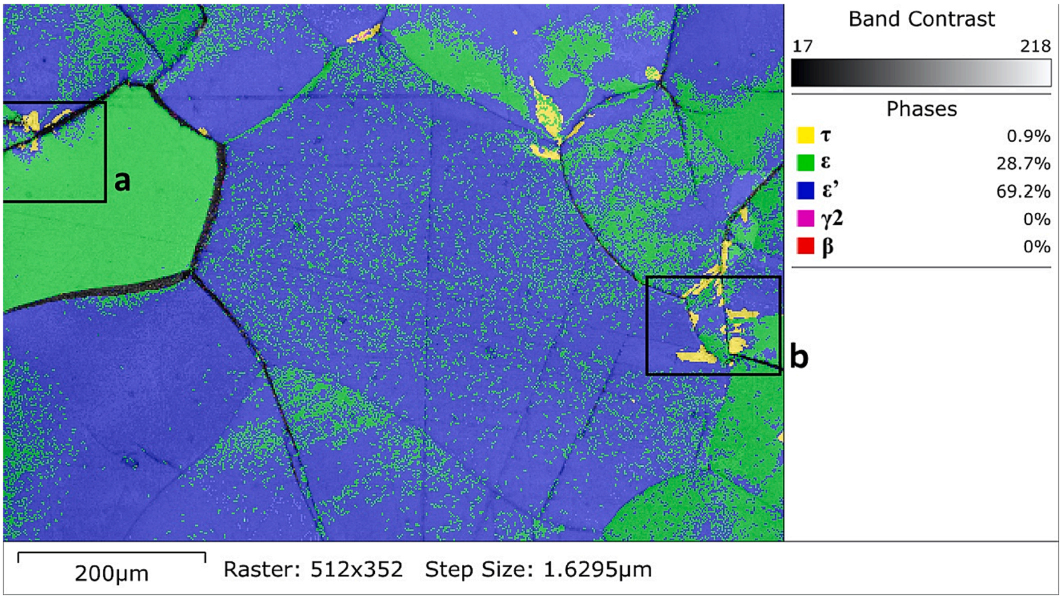

Fig. 8. EBSD image of 1 h 350 °C sample showing the phase fractions and parent ε phase grain boundaries. The boxes indicate the τ phase regions of interest shown in Fig. 11.

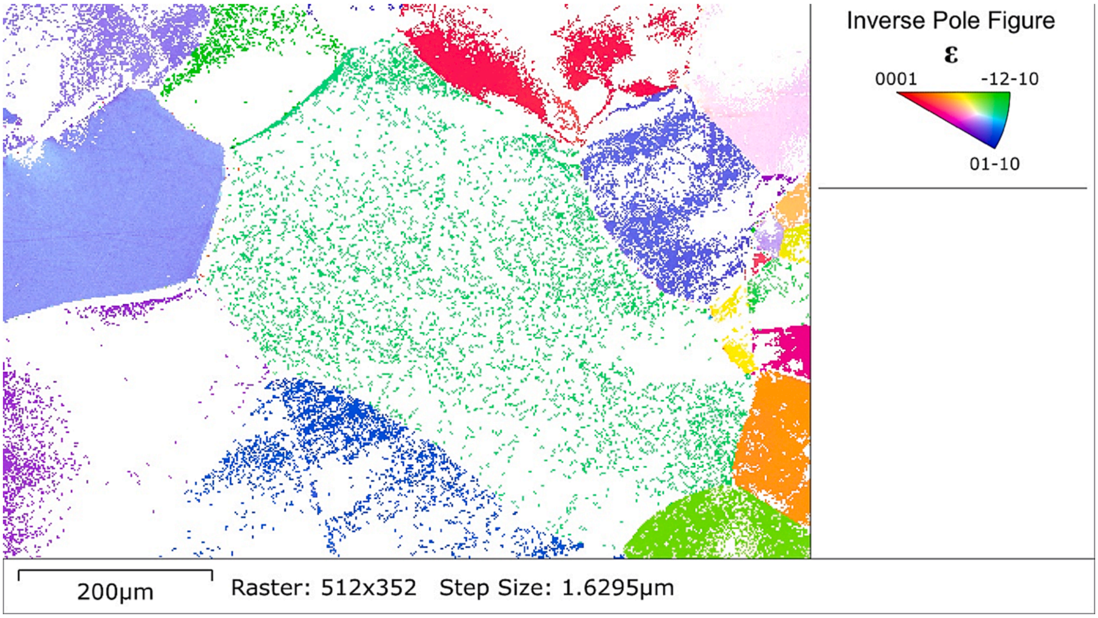

Fig. 9. EBSD image of 1 h 350 °C sample showing the ε phase inverse pole figure (IPF) orientation.

nature of ε' at low temperatures and its preference to form τ upon heating. There is a slight inflection point in Fig. 4 at ~75–100 °C, which if used as a linear extrapolation point to calculate T_c of the quenched-in phases (majority ε and minority ε') would give a T_c of roughly 300 °C, i.e., significantly lower than the T_c for τ. A more detailed study is required to identify the relative contributions between the different phases to this Curie behavior.

The E_a measured by Kissinger and FWO methods give average values of 142 ± 13 kJ/mol and 139 ± 8 kJ/mol, respectively, for the ε to ε' phase and average values of 155 ± 8 kJ/mol and 128 ± 10 kJ/mol, respectively, for the ε' to τ phase. This value for τ is lower than previous studies reporting ε to τ phase transformation values between 165 kJ/mol [2419] and 186 kJ/mol [21], within the accuracy of the Kissinger and FWO methods [43,44]. Therefore, the ordering transformation to ε' and the hybrid displacive-diffusional transformation to τ were shown to each have a lower activation energy than those reported for the τ phase alone without ε' phase ordering. This suggests a kinetic advantage for the ε to ε' to τ progression at temperatures less than 450 °C. In the absence of an activation energy barrier, direct transformation from ε phase to τ phase would be expected, since Table 2 shows a greater change in H for τ phase compared to ε' phase. However, with less thermal energy available below 450 °C, it is easier to overcome two smaller energy barriers (with ε' ordering) than one larger barrier (without ε' ordering) to form the τ phase, explaining the dominance of the displacive transformation mode at lower temperatures. This explains why, at 350 °C, τ phase growth is observed primarily into ε' regions and not ε phase regions via EBSD.

The FWO method does not show a dependence of E_a on α and is fairly constant within the margin of error; each phase transformation has a small increase to a maximum at α = 50 % and is lower at α = 10 % and 90 %. Thus, given the presence of some fraction of ε' nuclei already

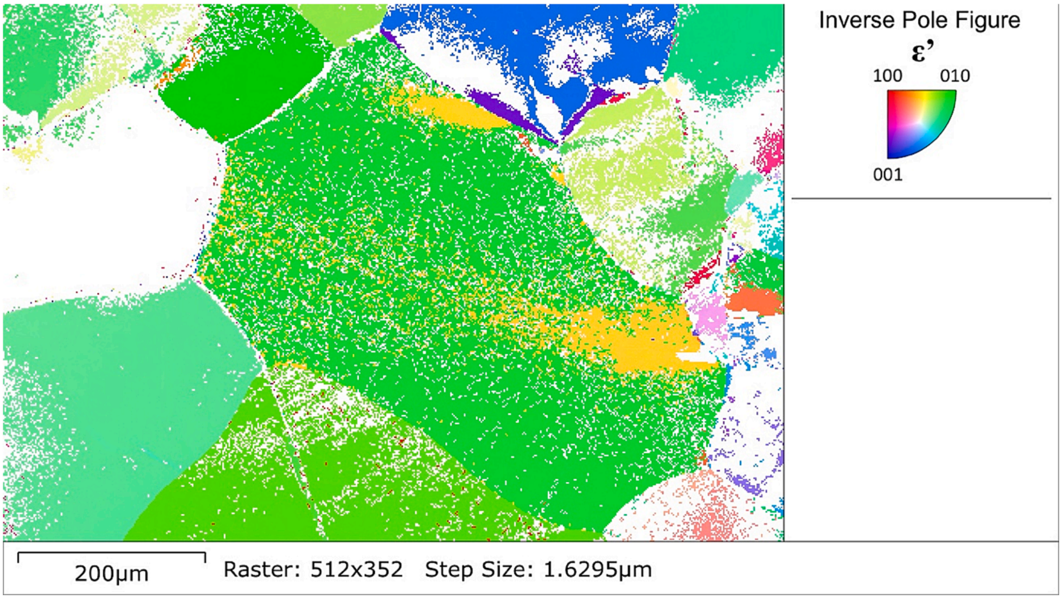

Fig. 10. EBSD image of 1 h 350 °C sample showing the ε’ phase IPF orientation.

present after quenching, the FWO method demonstrates that E_a does not significantly change from the beginning to the end of the ε’ phase transformation. This could be interpreted in one of two ways. First, it could indicate that the transformation to ε’ does not involve significant nucleation beyond the ε’ phase present in the as-quenched state and is only a process of growth of existing nuclei. Thus, E_a does not vary from $\alpha = 10\ \%$ to 90 % because the barrier to ε’ growth within large uniform ε phase grains is largely invariant. Second, it could indicate that nucleation does occur beyond the nuclei present in the as-quenched state, but that the E_a barrier to nucleation and growth processes are roughly the same. Further studies on ε phase free of ε’ nuclei are needed to confirm how much a role nucleation of the ε’ phase has on E_a compared to growth.

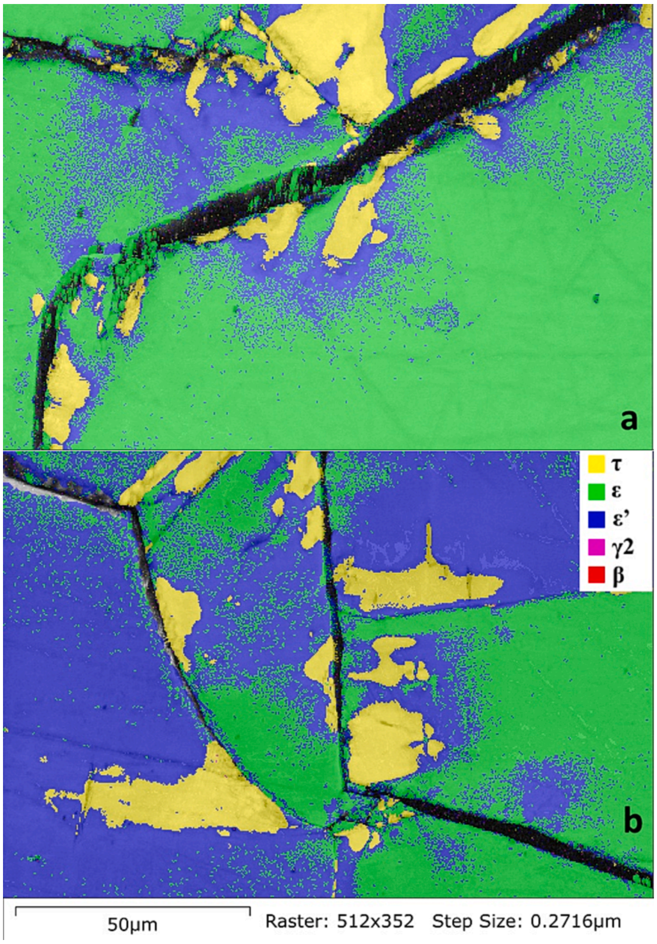

Fig. 11. Higher magnification EBSD phase map of Fig. 8 showing the τ phase growing behind an advancing ε’ phase into different parent ε phase grains (boxes a and b).

5. Conclusions

In-situ DSC, T-VSM, and HE-XRD were used to observe the phase transformation progression from ε to ε’ and then to τ and to confirm the formation of ε’ prior to τ for $Mn_{54}Al_{46}$. Isothermal annealing of quenched-in ε at 350 °C demonstrated that ε’ is FM, with a moderate H_{ci} of at least 50 kA/m. Using EBSD on 350 °C annealed samples, the τ phase was observed to nucleate on the previous grain boundaries of the parent ε phase and grow preferentially into the ε’ phase. A region of ε’ was observed between the τ and ε phases, showing that at 350 °C the τ phase has an energetic advantage growing into ε’ compared to ε and the displacive transformation mode dominates. DFT calculations confirmed the FM nature of ε’ and that the ε to ε’ to τ progression was energetically favorable. Calculated and measured ΔH values indicate that partial ordering of the ε’ phase occurs prior to τ formation. E_a values for ε’ and τ were similar, in the average range of ~140 kJ/mol for both phases. The ε to ε’ to τ progression of two transformations involving lower activation energies than the activation energy reported for τ alone demonstrate the kinetic advantage for why ε’ ordering is observed to occur prior to τ and why the τ phase preferentially grows into the ε’ phase regions. This study presents a framework to understand complex phase transformations by combining thermal, magnetic, and crystallographic measurements with DFT calculations. The methods of this study may be applicable to other $L1_0$ and metastable materials that experience an intermediate disorder–order phase transformation.

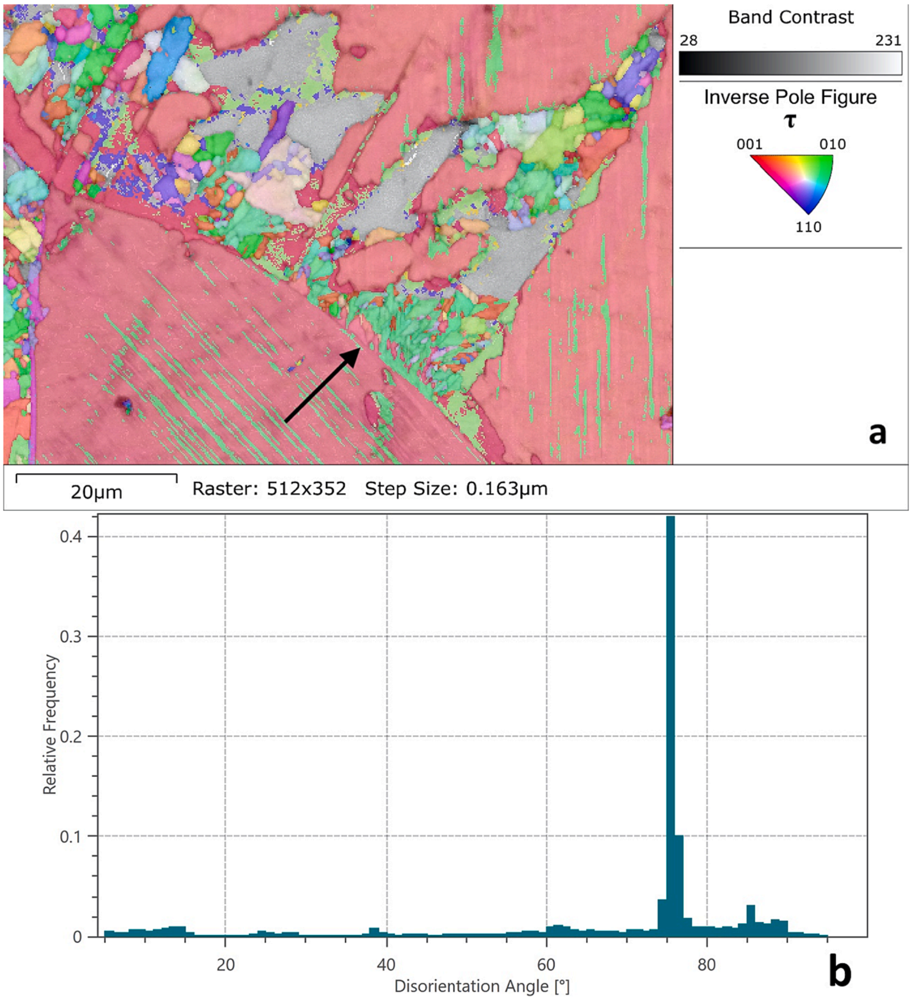

Fig. 12. (a) EBSD IPF map of 13 h 350 °C sample showing the growth of τ phase grains from a previous ε phase grain boundary (black arrow). The gray areas are untransformed ε. (b) Histogram of disorientations between neighboring τ phase grains: the peak at 76° corresponds to true twins.

Table 2

Calculated DFT values of H at −273.15 °C and magnetization for each phase of $Mn_{50}Al_{50}$. Mole refers to 1 mol of $Mn_{50}Al_{50}$ formula unit and ε is treated as the energy zero point.

Property	ε (AF)	ε' (FM)	τ (FM)
eV/atom (from ε) H	0	−0.103	−0.135
J/g (from ε) H	0	−243	−318
Change from parent phase (J/g) ΔH	–	−243	−75
Change from parent phase (kJ/mol) ΔH	–	−19.9	−6.14
Average Magnetization (μ_B/Mn atom)	–	2.107	2.264
Average Magnetization (μ_B/Al atom)	–	−0.044	−0.050
Total Average Magnetization (μ_B/atom)	–	1.032	1.107

Table 3

Measured DSC values for E_a from Kissinger method and FWO method for percent transformed fraction, α. DSC heating rates used were 5, 10, 12, 15, 60 and 80 °C/min on $Mn_{54}Al_{46}$. Mole refers to 1 mol of $Mn_{54}Al_{46}$ formula unit.

Activation Energy E_a (units)	ε to ε'	ε' to τ
Kissinger Method (kJ/mol)	142 ± 13	155 ± 8
FWO α = 10 % (kJ/mol)	141 ± 4	119 ± 7
FWO α = 25 % (kJ/mol)	147 ± 4	136 ± 5
FWO α = 50 % (kJ/mol)	144 ± 3	139 ± 4
FWO α = 75 % (kJ/mol)	138 ± 5	129 ± 4
FWO α = 90 % (kJ/mol)	126 ± 7	117 ± 5
FWO Average (kJ/mol)	139 ± 8	128 ± 10

Table 4

DSC determined ΔH values for energy exothermically released (negative sign) from the low-temperature peak (ε to ε') and high-temperature peak (ε' to τ) DSC heating rates used were 5, 10, 12, 15, 60 and 80 °C/min on $Mn_{54}Al_{46}$. Mole refers to 1 mol of $Mn_{54}Al_{46}$ formula unit.

Energy (units)	ε to ε'	ε' to τ
ΔH (J/g)	−44 ± 8	−40 ± 6
ΔH (kJ/mol)	−3.70 ± 0.67	−3.37 ± 0.51

CRediT authorship contribution statement

Thomas Keller: Conceptualization, Methodology, Validation, Formal analysis, Investigation, Writing – original draft, Writing – review & editing, Visualization, Supervision, Project administration. **Dylan Barbagallo:** Methodology, Software, Validation, Formal analysis, Investigation, Data curation, Writing – review & editing. **Natalya Sheremetyeva:** Methodology, Software, Validation, Formal analysis, Investigation, Data curation, Writing – review & editing. **Tushar Kanti Ghosh:** Methodology, Software, Validation, Formal analysis, Investigation, Data curation, Writing – review & editing, Visualization. **Katherine S. Shanks:** Methodology, Investigation, Resources. **Geoffroy Hautier:** Conceptualization, Methodology, Writing – review & editing, Supervision, Project administration, Funding acquisition. **Ian Baker:** Conceptualization, Methodology, Writing – review & editing, Supervision, Project administration, Funding acquisition.

Declaration of Competing Interest

The authors declare that they have no known competing financial interests or personal relationships that could have appeared to influence the work reported in this paper.

Data availability

Data will be made available on request.

Acknowledgements

This work was supported by the National Science Foundation under awards 1852529 and 2032592. This work is also based on research conducted at the Center for High-Energy X-ray Sciences (CHEXS), which is supported by the at National Science Foundation (BIO, ENG and MPS Directorates) under award DMR-1829070.

References

[1] T. Keller, I. Baker, Manganese-based permanent magnet materials, Prog. Mater Sci. 124 (2022), 100872, https://doi.org/10.1016/j.pmatsci.2021.100872.

[2] F. Jiménez-Villacorta, J.L. Marion, J.T. Oldham, M. Daniil, M.A. Willard, L. H. Lewis, Magnetism-structure correlations during the ε→τ transformation in Rapidly-Solidified mnal nanostructured alloys, Metals (Basel) 4 (2014) 8–19, https://doi.org/10.3390/met4010008.

[3] C.T. Lee, K.H. Han, I.H. Kook, W.K. Choo, Phase and lattice parameter relationships in rapidly solidified and heat-treated (Mn0.53Al0.470)100-xCx pseudo-binary alloys, J. Mater. Res. 7 (1992) 1690–1695, https://doi.org/10.1557/JMR.1992.1690.

[4] S. Kojima, T. Ohtani, N. Kato, K. Kojima, Y. Sakamoto, I. Konno, M. Tsukahara, T. Kubo, Crystal transformation and orientation of Mn-Al-C hard magnetic alloy, 768 (2008) 768–769. doi: 10.1063/1.30281.

[5] J.M.K. Wiezorek, A.K. Kulovits, C. Yanar, W.A. Soffa, Grain boundary mediated displacive-diffusional formation of τ-phase MnAl, Metall. Mater. Trans. A 42 (2011) 594–604, https://doi.org/10.1007/s11661-010-0308-1.

[6] P.Z. Si, H.D. Qian, C.J. Choi, J. Park, S. Han, H.L. Ge, K.P. Shinde, In situ observation of phase transformation in MnAl(C) magnetic materials, Materials. 10 (2017) 1016–1026, https://doi.org/10.3390/ma10091016.

[7] Y. Jia, H. Ding, Y. Wu, J. Wang, H. Wu, T. Ma, S. Zhao, K.P. Skokov, A. Aubert, F. Maccari, O. Gutfleisch, Y. Xu, J. Niu, B. Qiao, S. Zhao, C. Jiang, On the ε → τ phase transformation and twinning in L10−MnAl alloys, Acta Mater. 232 (2022), 117892, https://doi.org/10.1016/j.actamat.2022.117892.

[8] C. Yanar, J.M.K. Wiezorek, V. Radmilovic, W.A. Soffa, Massive transformation and the formation of the ferromagnetic $L1_0$ phase in manganese-aluminum-based alloys, Metall. Mater. Trans. A 33 (2002) 2413–2423, https://doi.org/10.1007/s11661-002-0363-3.

[9] C. Zhang, T. Zhang, J. Wang, S. Zhao, Y. Wu, C. Jiang, Anisotropic single-variant of (Mn54Al46)97C3, Scr. Mater. 143 (2018) 72–76, https://doi.org/10.1016/j.scriptamat.2017.09.008.

[10] P. Müllner, B.E. Bürgler, H. Heinrich, A.S. Sologubenko, G. Kostorz, Observation of the shear mode of the ε → τ phase transformation in a Mn-Al-C single crystal, Philos. Mag. Lett. 82 (2002) 71–79, https://doi.org/10.1080/09500830110103225.

[11] D.P. Hoydick, E.J. Palmiere, W.A. Soffa, On the formation of the metastable $L1_0$ phase in manganese-aluminum-base permanent magnet materials, Scr. Mater. 36 (1997) 151–156, https://doi.org/10.1016/S1359-6462(96)00356-9.

[12] D.P. Hoydick, E.J. Palmiere, W.A. Soffa, Microstructural development in MnAl-base permanent magnet materials: New perspectives, J. Appl. Phys. 81 (1997) 5624–5626, https://doi.org/10.1063/1.364619.

[13] D. Palanisamy, S. Singh, C. Srivastava, G. Madras, K. Chattopadhyay, Predicting Pathways for Synthesis of Ferromagnetic τ Phase in Binary Heusler Alloy Al-55 pct Mn Through Understanding of the Kinetics of ε–τ Transformation, Metall. Mater. Trans. A 47 (2016) 6555–6568, https://doi.org/10.1007/s11661-016-3756-4.

[14] J.J. van den Broek, H. Donkersloot, G. van Tendeloo, J. van Landuyt, Phase transformations in pure and carbon-doped $Al_{45}Mn_{55}$ alloys, Acta Metall. 27 (1979) 1497–1504, https://doi.org/10.1016/0001-6160(79)90172-X.

[15] A.S. Sologubenko, P. Müllner, H. Heinrich, M. Woligarten, G. Kostorz, The effect of composition and stress on the selection of epsilon to tau transformation modes in MnAl-C, Journale De Physique IV 112 (2003) 1071–1074.

[16] V. Øygarden, J. Rial, A. Bollero, S. Deledda, Phase-pure τ-MnAlC produced by mechanical alloying and a one-step annealing route, J. Alloy. Compd. 779 (2019) 776–783, https://doi.org/10.1016/j.jallcom.2018.11.175.

[17] H. Fang, J. Cedervall, F.J.M. Casado, Z. Matej, J. Bednarcik, J. Ångström, P. Berastegui, M. Sahlberg, Insights into formation and stability of τ-MnAlZx (Z = C and B), J. Alloy. Compd. 692 (2017) 198–203, https://doi.org/10.1016/j.jallcom.2016.09.047.

[18] V.M. Gundyrev, M.A. Uimin, A.E. Ermakov, O.B. Andreeva, Transformation in MnAl-C Alloys, Physica Status Solidi (a). 91 (1985) K55–K58, https://doi.org/10.1002/pssa.2210910152.

[19] W. Lu, J. Niu, T. Wang, K. Xia, Z. Xiang, Y. Song, Z. Mi, W. Zhang, W. Tian, Y. Yan, Phase transformation kinetics and microstructural evolution of MnAl permanent magnet alloys, J. Alloy. Compd. 685 (2016) 992–996, https://doi.org/10.1016/j.jallcom.2016.06.285.

[20] P.Z. Si, H.D. Qian, C.J. Choi, J. Park, H.L. Ge, A novel method for measuring the phase transformation temperature and enhanced coercivity in cold-rolled MnAlCx (x = 0–5) alloys, J. Magn. Magn. Mater. 451 (2018) 540–545, https://doi.org/10.1016/j.jmmm.2017.11.094.

[21] I. Janotová, P. Švec, P. Švec, I. Mat'ko, D. Janičkovič, J. Zigo, M. Mihalkovič, J. Marcin, I. Škorvánek, Phase analysis and structure of rapidly quenched Al-Mn systems, J. Alloy. Compd. 707 (2017) 137–141, https://doi.org/10.1016/j.jallcom.2016.11.171.

[22] A.M. Genc, O. Acar, S. Turan, I. Kalay, U. Savacı, Y.E. Kalay, Investigation of phase selection hierarchy in Mn–Al alloys, Intermetallics (barking) 115 (2019), 106617, https://doi.org/10.1016/j.intermet.2019.106617.

[23] D. Palanisamy, C. Srivastava, G. Madras, K. Chattopadhyay, High-temperature transformation pathways for metastable ferromagnetic binary Heusler (Al–55 at.% Mn) alloy, J. Mater. Sci. 52 (2017) 4109–4119, https://doi.org/10.1007/s10853-016-0673-2.

[24] A.D. Crisan, F. Vasiliu, R. Nicula, C. Bartha, I. Mercioniu, O. Crisan, Thermodynamic, structural and magnetic studies of phase transformations in MnAl nanocomposite alloys, Mater Charact 140 (2018) 1–8, https://doi.org/10.1016/j.matchar.2018.03.034.

[25] Y. Chen, Q. Wang, Thermal oxidative degradation kinetics of flame-retarded polypropylene with intumescent flame-retardant master batches in situ prepared in twin-screw extruder, Polym. Degrad. Stab. 92 (2007) 280–291, https://doi.org/10.1016/j.polymdegradstab.2006.11.004.

[26] G. Kresse, D. Joubert, From ultrasoft pseudopotentials to the projector augmented-wave method, Phys. Rev. B 59 (1999) 1758–1775, https://doi.org/10.1103/PhysRevB.59.1758.

[27] G. Kresse, J. Furthmüller, Efficient iterative schemes for ab initio total-energy calculations using a plane-wave basis set, Phys. Rev. B 54 (1996) 11169–11186, https://doi.org/10.1103/PhysRevB.54.11169.

[28] G. Kresse, J. Furthmüller, Efficiency of ab-initio total energy calculations for metals and semiconductors using a plane-wave basis set, Comput. Mater. Sci 6 (1996) 15–50, https://doi.org/10.1016/0927-0256(96)00008-0.

[29] G. Kresse, J. Hafner, VASP the Guide (Vienna University of Technology, Vienna, 2001), Phys. Rev B. 47 (1993) 0927–0256.

[30] Q. Zeng, I. Baker, J.B. Cui, Z.C. Yan, Structural and magnetic properties of nanostructured Mn-Al-C magnetic materials, J. Magn. Magn. Mater. 308 (2007) 214–226, https://doi.org/10.1016/j.jmmm.2006.05.032.

[31] A. Zunger, S.-H. Wei, L.G. Ferreira, J.E. Bernard, Special Quasirandom Structures, Phys. Rev. Lett. 65 (1990) 353.

[32] A. Van De Walle, G. Ceder, Automating First-Principles Phase Diagram Calculations, J. Phase Equilib. 23 (2002) 348.

[33] A. Van De Walle, M. Asta, G. Ceder, The Alloy Theoretic Automated Toolkit: A User Guide, Calphad 26 (2002) 539–553.

[34] A. Van De Walle, P. Tiwary, M. De Jong, D.L. Olmsted, M. Asta, A. Dick, D. Shin, Y. Wang, L.-Q. Chen, Z.-K. Liu, Efficient stochastic generation of special quasirandom structures, Calphad 42 (2013) 13–18, https://doi.org/10.1016/j.calphad.2013.06.006.

[35] A. Van De Walle, Multicomponent multisublattice alloys, nonconfigurational entropy and other additions to the Alloy Theoretic Automated Toolkit, Calphad 33 (2009) 266–278, https://doi.org/10.1016/j.calphad.2008.12.005.

[36] H.E. Kissinger, Reaction Kinetics in Differential Thermal Analysis, Anal. Chem. 29 (1957) 1702–1706. https://pubs.acs.org/sharingguidelines.

[37] J.H. Flynn, L.A. Wall, General Treatment of the Thermogravimetry of Polymers, J. Res. National Bureau of Standards – A. Phys. Chem. 70A (1966) 487.

[38] T. Ozawa, A New Method of Analyzing Thermogravimetric Data, Bull. Chem. Soc. Jpn 38 (1965) 1881–1886.

[39] T.H. Grgurić, D. Manasijević, S. Kožuh, I. Ivanić, I. Anžel, B. Kosec, M. Bizjak, E. G. Bajsić, L. Balanović, M. Gojić, The effect of the processing parameters on the martensitic transformation of Cu-Al-Mn shape memory alloy, J. Alloy. Compd. 765 (2018) 664–676, https://doi.org/10.1016/j.jallcom.2018.06.250.

[40] J.H. Park, Y.K. Hong, S. Bae, J.J. Lee, J. Jalli, G.S. Abo, N. Neveu, S.G. Kim, C. J. Choi, J.G. Lee, Saturation magnetization and crystalline anisotropy calculations for MnAl permanent magnet, J. Appl. Phys. 107 (2010) 1–4, https://doi.org/10.1063/1.3337640.

[41] Z. Xiang, X. Wang, Y. Song, L. Yu, E. Cui, B. Deng, D. Batalu, W. Lu, Effect of cooling rates on the microstructure and magnetic properties of MnAl permanent magnetic alloys, J. Magn. Magn. Mater. 475 (2019) 479–483, https://doi.org/10.1016/j.jmmm.2018.12.003.

[42] D.A. Porter, K.E. Easterling, M.Y. Sherif, Phase Transformations in Metals and Alloys, 3rd ed., CRC Press, Boca Raton, FL, 2009.

[43] R.L. Blaine, H.E. Kissinger, Homer Kissinger and the Kissinger equation, Thermochim. Acta 540 (2012) 1–6, https://doi.org/10.1016/j.tca.2012.04.008.

[44] M.J. Starink, The determination of activation energy from linear heating rate experiments: A comparison of the accuracy of isoconversion methods, Thermochim Acta 404 (2003) 163–176, https://doi.org/10.1016/S0040-6031(03)00144-8.